Investigating Abiotic Sources of Spectral Variability From Multitemporal Hyperspectral Airborne Acquisitions Over the French Guyana Canopy

Colin Prieur, Antony Laybros, Giovanni Frati, Daniel Schläpfer, Jocelyn Chanussot, Grégoire Vincent

Investigating Abiotic Sources of Spectral Variability From Multitemporal Hyperspectral Airborne Acquisitions Over the French Guyana Canopy

Colin Prieur, Antony Laybros, Giovanni Frati, Daniel Schläpfer, Jocelyn Chanussot, and Grégoire Vincent

***Abstract*—Classifiers trained on airborne hyperspectral imagery are proficient in identifying tree species in hyperdiverse tropical rainforests. However, spectral fluctuations, influenced by intrinsic and environmental factors, such as the heterogeneity of individual crown properties and atmospheric conditions, pose challenges for large-scale mapping. This study proposes an approach to assess the instability of airborne imaging spectroscopy reflectance in response to environmental variability. Through repeated overflights of two tropical forest sites in French Guiana, we explore factors that affect the spectral similarity between dates and acquisitions. By decomposing acquisitions into subsets and analyzing different sources of variability, we analyze the stability of reflectance and various vegetation indices with respect to specific sources of variability. Factors such as the variability of the viewing and sun angles or the variability of the atmospheric state shed light on the impact of sources of spectral instability, informing processing strategies. Our experiments conclude that the environmental factors that affect the canopy reflectance the most vary according to the considered spectral domain. In the short wave infrared (SWIR) domain, solar angle variation is the main source of variability, followed by atmospheric and viewing angles. In the visible and near infrared (VNIR) domain, atmospheric variability dominates, followed by solar angle and viewing angle variabilities. Despite efforts to address these variabilities, significant spectral instability persists, highlighting the need for more robust representations and improved correction methods for reliable species-specific signatures.**

***Index Terms*—Hyperspectral imaging, reflectivity, spectroscopy, vegetation mapping.**

I. Introduction

TROPICAL forests and their biodiversity are key markers for the climate change and are under critical threat because of an increased pressure stemming from human direct or indirect influence. Effective high-throughput remote sensing tools are hence crucial to document the floristic compositions of inaccessible environments and their evolution [1], [2].

Field identifications, while fundamental, are expensive, laborious, slow, and even potentially detrimental to these areas. Road construction and survey trails, commonly required for ground-based botanical identification, not only disturb forests in their own right, but also improve the access of poachers and illegal loggers [3], [4], [5]. Also, they do not scale up for the repeated monitoring of large areas.

Data quality is key for the effectiveness of remote sensing approaches in identifying plant species. RGB images show promise in species discrimination, the very high spatial resolution compensating for the spectral limitations [6], [7]. However, large-area mapping with very high-resolution drones also faces challenges due to limited autonomy and computational costs.

In tropical forests, where tree species richness can exceed 300 species per hectare [8], [9], hyperspectral airborne imaging, offering metric resolution imagery, is wellsuited for canopy species mapping [10], [11], [12], [13].

However, challenges arise from sensor sensitivity to acquisition context, which compromises the transferability of the identification technique [12], [13], [14], [15].

The effects of bidirectional reflectance distribution function (BRDF) on the classification performances of temperate tree species were analyzed by [16], highlighting the importance of incorporating BRDF corrections [13], [15]. Furthermore, Laybros et al. [12] reported a loss in species classification performances of ca. 10 points when a classifier trained on one date was applied to hyperspectral imagery collected the following day.

Failure to address spectral variability stemming from environmental conditions can impede species identification efforts. This variability poses a challenge in the implementation of large-scale identification models, as classifiers struggle to maintain performance across different acquisition contexts [16], even for the same area imaged on different dates [12]. This necessitates model retraining and in situ ground-truthing for each acquisition and study area, contradicting the technology's primary benefit. However, different spectral signal representations may exhibit differing levels of resilience to this variability [13], [16].

Two forms of spectral variability are commonly distinguished, [17], [18].

1) The "intrinsic" or biotic variability of vegetation reflects differences in phenological stage, water and nutrient content, leaf size, density, and arrangement, influencing the optical properties [17], [18], [19]. These characteristics may change over time for an individual tree crown but will also show variability within an individual tree crown at any point in time. Previous research using models like

Received 16 April 2024; revised 18 September 2024; accepted 23 September 2024. Date of publication 7 October 2024; date of current version 23 October 2024. *(Corresponding author: Colin Prieur.)*

Colin Prieur, Giovanni Frati, and Grégoire Vincent are with the AMAP, University of Montpellier, CIRAD, CNRS, INRAE, IRD, 34980 Montpellier, France (e-mail: colin.prieur@gmail.com).

Antony Laybros is with the ONF, AMAP, 97300 Montpellier, France.

Daniel Schläpfer is with the ReSe Applications LLC, 9500 Wil, Switzerland.

Jocelyn Chanussot is with the Universite Grenoble Alpes, Inria, CNRS, Grenoble INP, LJK, 38000 Grenoble, France.

Digital Object Identifier 10.1109/JSTARS.2024.3475050

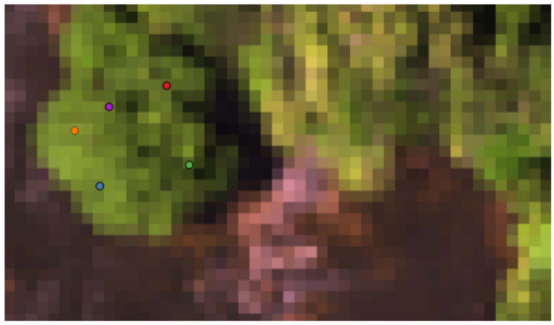

(a)

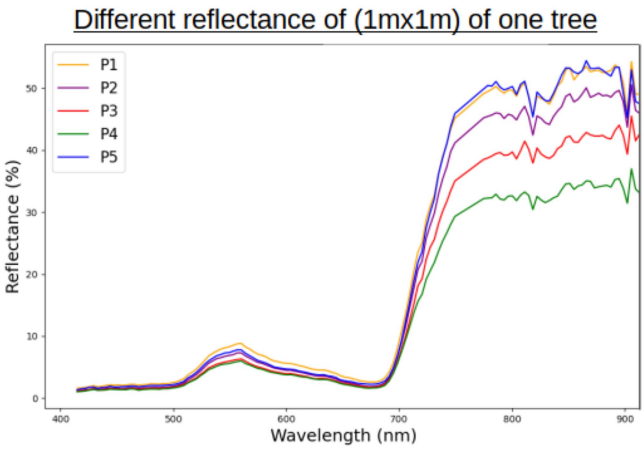

(b)

Fig. 1. (a) Location of the pixels considered within one tree for a single acquisition. (b) Spectra of the considered pixels.

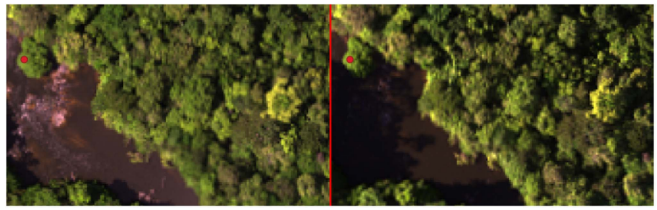

Fig. 2. Different acquisitions of the same area in RGB false color from an hyperspectral acquisition.

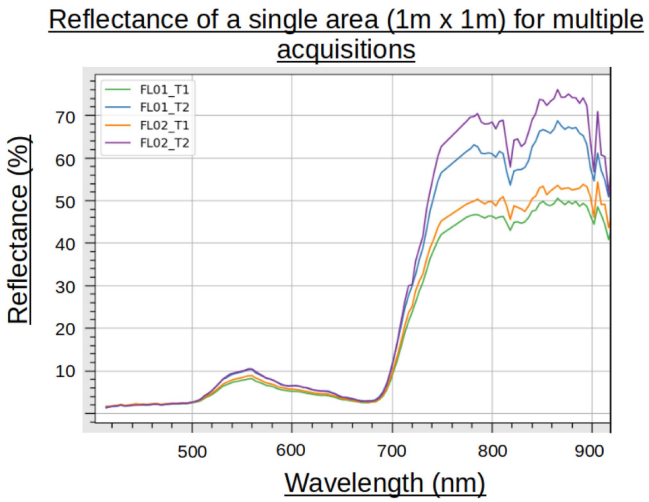

Fig. 3. Several spectra of the same area (red dot in Fig. 2) given different hyperspectral acquisitions.

MODTRAN [17], [18], [19] and the PROSPECT [20], [21] and SAIL model [22] and their combination, PROSAIL [23] has explored the effects of leaf and canopy properties such as leaves chemical composition, leaf tissue structure, and leaf spatial arrangement on species' spectral signatures [19], [24]. Despite its importance, the phenology of tropical forests is poorly documented, which complicates species identification [25]. Intrinsic variability is evident within single tree crowns (see Fig. 1), largely due to their 3-D nature and multiple scattering effects, which challenge per-pixel modeling.

2) The "environmental" or abiotic variability refers to each pixel's spectrum sensitivity to acquisition conditions. High-resolution airborne imagery's radiance at the sensor is affected by factors related to atmospheric conditions (aerosols, water vapor, cloud cover), solar illumination (irradiance angle, and diffuse illumination) [17], [26]. Remote sensing tool development is closely linked to progress made in atmospheric correction routines [26], [27], [28], aiming for calibrated spectral representations validated with in situ acquisitions [26], [29].
However, atmospheric corrections aim at estimating the in situ reflectance [29], which varies with illumination conditions [30], reflectance anisotropy [14], [31], [32], [33], [34], and adjacency effects [35]. The abiotic variability, highlighted in studies [12], [16], and [36], emerges in spectral plots of the same pixel between acquisitions (see Figs. 2 and 3).

The design of a scalable procedure for species identification encounters two challenges.

The first challenge is related to intrinsic variability and pervades any species identification endeavor [11], [12], [37]. Utilizing airborne hyperspectral technology alongside a representative ground-truth of tropical forest botanical variability offers promise in overcoming this hurdle, with identification method robustness evaluated across diverse test datasets [11], [12], [37]. The second challenge relates to spectral representation resilience amid abiotic variability. Despite atmospheric correction addressing this variability, the performance of hyperspectral datasets hinges on acquisition parameters [12], [16]. Vögtli et al. [36] investigates spectral index and band sensitivity using the ATCOR4 and BREFCOR methods [26], [31]. While atmospheric correction extracts intrinsic pixel properties, correcting BRDF effects in tree crowns remains problematic due to leaf and branch orientation [38], [39]. Arguably, the correction of BRDF effects in tree crowns is an ill-posed problem that cannot be solved at high resolution due to the undefined orientation of leaves and tree branches. Only the correction of illumination differences is theoretically feasible on a per-pixel basis, provided an accurate estimate of the illumination factors can be done, as demonstrated by Carmon et al. [40].

Environmental variability has been addressed in different contexts.

1) Techniques for reducing spectral variability in material identification, outlined in [17], involve encoding resilient representations through physics-based corrections or statistical methods, and integrating a priori assumptions about target variability.
2) Spectral unmixing methodologies [18] incorporate spectral variability by employing freedom coefficients to address spectral mixtures. Other approaches use simulators [23], [41] to expand spectral libraries with multiple iterations of the same material under diverse acquisition conditions, improving the robustness of unmixing algorithms by capturing varied spectral responses across environmental contexts.

This study evaluates the resilience of hyperspectral imagery to abiotic variability in two sites of French Guiana. We consider two response variables: 1) reflectance spectra produced from the Atcor4 flat terrain algorithm; and 2) vegetation indices derived from selected bands of the spectra: the normalized vegetation difference index (NDVI) [42], [43], [44], the chlorophyll index (CHL) [45], [46], the CARotenoid index (CAR) [45], [46], and the equivalent water thickness (EWT) index [45], [47]. We evaluate the relative importance of factors such as viewing and solar angles, atmosphere, and illumination variations.

Hyperspectral image strips are decomposed into pixel pairs from identical coordinates. Spectral consistency is measured via bandwise correlation coefficients and spectral indices. The influence of coregistration errors is investigated through synthetic datasets, comparing their variability with real acquisitions.

In this study, we aim to test several hypotheses regarding spectral variability in airborne hyperspectral imagery.

1) Specifically, we seek to determine whether spectral variability between acquisition dates surpasses spatial variability within a given species for one given acquisition.
2) Additionally, we aim to assess the superior importance of solar angle variability compared to viewing angle variability on the BRDF effects.
3) Lastly, we investigate whether vegetation indices exhibit greater stability compared to raw reflectance, given their design to capture biophysical canopy parameters that are supposed constant across acquisitions.

The rest of this article is organized as follows. Section II details the study sites, data sources, preprocessing operations, spectral coherence metrics, and how the influence of the different sources of variability is highlighted. Section III presents different correlation per bands across subdatasets and the influence of sources of variability over the spectral domain and spectral indices. Section IV includes discussion and limitations of our work. Finally, Section V concludes this article.

II. Material and Method

A. Study Sites

Two natural forested landscapes in French Guiana were considered for this study: Paracou and Nouragues, respectively.

The Paracou research station is located in the north of French Guiana (5°16' N, 52°55' W), about 15 km from the coast [48]. The annual average temperature is 26 °C with a variation of ± 1 °C. The rainfall is around, 2875 ± 510 mm per year [48]. The Paracou site is a hilly area, its altitude varies from 5 m to about 45 m above sea level [48].

The Nouragues station is part of the Nouragues nature reserve located in the center-east of French Guiana, 100 km from the coast (4°05' N, 52°40' W) [49]. The average rainfall is 2990 mm per year [49]. The relief is made up of hills and plateaus. The elevation of the site varies from 60 to 420 m at the top of an inselberg.

B. Data Sources

Hyperspectral data were acquired by Hytech-Imaging using two sensors: Hyspex VNIR-1600 and Hyspex SWIR-384me (Hyspex NEO, Norway), with a combined 17° field of view (FOV). At the same time, a LiDAR laser scanner Riegl LMSQ780 acquired data point clouds. The VNIR sensor covers the range from 414 to 993 nm, discretized into 160 spectral bands with a spectral sampling of 3.7 nm. The SWIR-384me sensor covers the range from 976 to 2512 nm discretized into 288 spectral bands and 5.45 nm spectral sampling. The final ground sampling distance (GSD) was 1 m for VNIR and 2 m for SWIR data.

A NIR camera and an RGB camera, respectively, IXA-R 160 and iXU 180 from Phase One were added to the payload to produce very high resolution imaging of the acquisition (10 cm GSD). The NIR acquisition resampled to the hyperspectral VNIR resolution was later used to reproject flight lines into a common mosaic (Section II-B3).

1) Date and Time of Acquisitions: Overflights of Nouragues took place on 21 September 2016, and 22 September 2016. The first acquisition started at 2:39 P.M. and finished at 4:38 P.M., equivalent to 1:59 P.M. and 3:59 P.M. in solar hour. A low proportion of cloud shadows was present (see Table I). The second acquisition started at 2:38 P.M. and finished at 4:38 P.M., equivalent to 1:58 P.M. and 3:58 P.M. in solar hour. A greater proportion of shadows was present on the second day (see Table I), flight geometry is presented in Fig. 4. The flight plans were similar, but the first overflight of this area started in the west and ended in the east, while the second flight started in the east and ended in the west.

Overflights of the Paracou site took place on 19 September 2016 and 20 September 2016. The first acquisition started at 1:12 P.M. and finished at 3:38 P.M. local time, equivalent to 00:32 P.M. and 2:58 P.M. in solar hour, starting on the western side of the site (see Table I). The second acquisition started at 2:14 P.M. and finished at 3:00 P.M., equivalent to 1:34 P.M. and 2:20 P.M. in solar hour, covering a smaller area, about one third of the area imaged on the first date; flight geometry is presented in Fig. 5 and Table I.

2) Corrections Applied: The hyperspectral images were radiometrically corrected using static calibration parameters of the manufacturer taking into account the dark signal, the bad pixels, and the spectral response functions (SRF) depending on the field of view (FOV).

TABLE I
OVERFLIGHTS CHARACTERISTICS; THE PROPORTION OF CLOUD SHADOW IS BASED ON VISUAL DELINEATION OF SHADOWS ON THE HYPERSPECTRAL IMAGERY

Date	Site	Area imaged Km²	Start time (UT -3, PM)	End time (UT -3, PM)	Altitude above the sea level	Clear sky pixels (%)	Flight lines acquired from
09/21/2016	Nouragues	24	2:39	4:38	1100	61.3	West → East
09/22/2016	Nouragues	24	2:38	4:38	1100	52.9	East → West
09/19/2016	Paracou	10	1:12	3:38	920	61.8	West → East
09/20/2016	Paracou	3	2:14	3:00	920	52.0	West → East

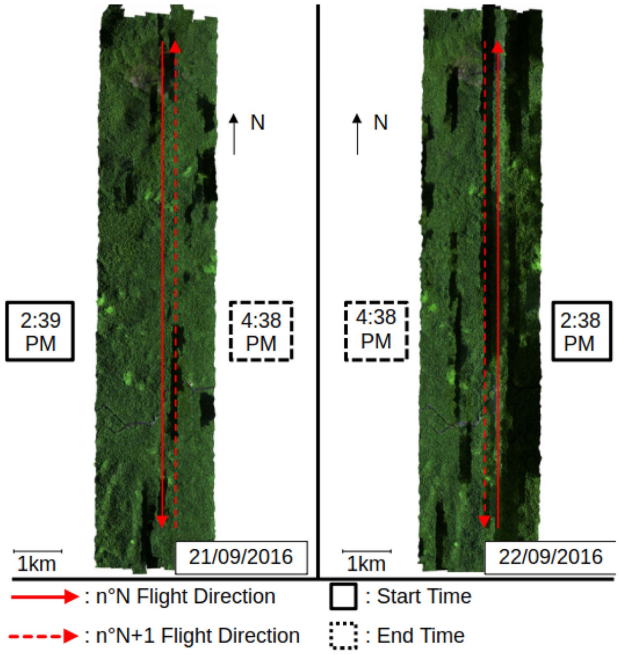

Fig. 4. Flight schedule over an RGB mosaic (1 m GSD) of Nouragues for the first date and second date of acquisition.

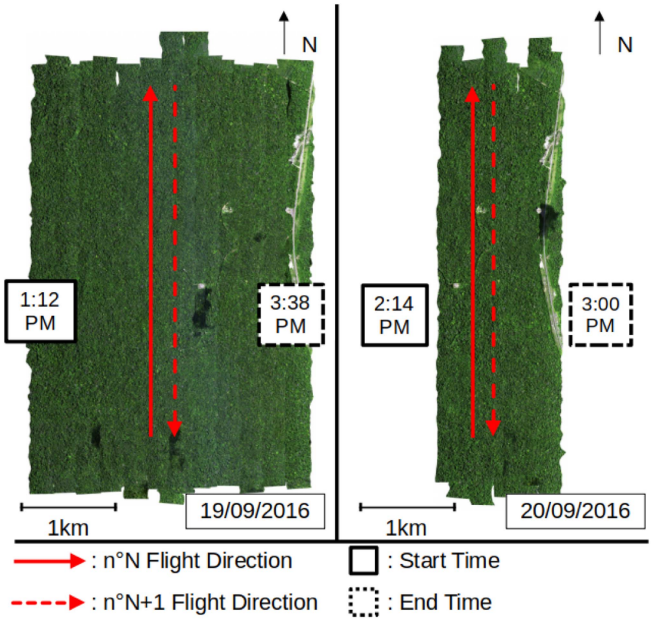

Fig. 5. Flight schedule over an RGB mosaic (1 m GSD) of Paracou for the first date and second date of acquisition.

Hyperspectral radiance images were then orthorectified and georeferenced at 1 m spatial resolution for the VNIR sensor and at 2 m spatial resolution for the SWIR sensor with PARGE software [50]. A 1 m-DSM (digital surface model) was produced from the LiDAR point cloud by selecting the highest return per 1 m grid cell. The DSM was used for a refined orthorectification. However, orthorectified flight lines still showed coregistration errors between overlapping flight lines that were locally greater than one pixel, inducing a coregistration error of more than 1 or 2 m for the VNIR and SWIR acquisitions, respectively. These errors can be attributed to the intrinsic error of the Lidar surface model created from the point cloud of a tree canopy, i.e., to our knowledge there is no method available to determine the radiometrically relevant surface from point clouds from a 3-D canopy structure.

Each flight line was corrected using ATCOR-4 software assuming flat terrain to remove atmospheric perturbations [26]. The same atmospheric lookup table file considering rural aerosol and the water vapor column was calculated automatically from imagery using the 820 nm water vapor absorption band for each study area and date.

As the aircraft flew between 920 and 1100 m altitude, the water vapor column was estimated at an altitude of 1000 m. Atmospheric correction yielded estimates globally consistent with field measurements taken during the campaign, which are accessible using the following link.[1] Registered aerosol optical thickness (AOT) from a Helio-photometer CIMEL located at the drop zone north of the study area (Inselberg camp) in Nouragues and on an open area in Paracou was below 0.2 for the 500 nm band and equal to 0.143 on average for both days. The measured daily average water column was 3.5 and 3.75 cm for the first and second dates of acquisition, which suggests a high level of perturbation due to water content [51].

According to [51], the amount of aerosol optical thickness can be considered low on average (less than 0.18) at 500 nm on both days at both study sites and low to moderate (less than 0.25) for the worst conditions, which showed an AOT of 0.2 for the 500 nm band. A constant rural AOT estimate per date was considered for the atmospheric correction [26] (rather than a spatially explicit version), [52].

3) Coregistration Operation: As mentioned in Section II-B2, images projected onto the surface model still suffered from a spatial registration error of about one pixel.

[1][Online]. Available: https://aeronet.gsfc.nasa.gov/cgi-bin/draw_ map_ display_aod_v3

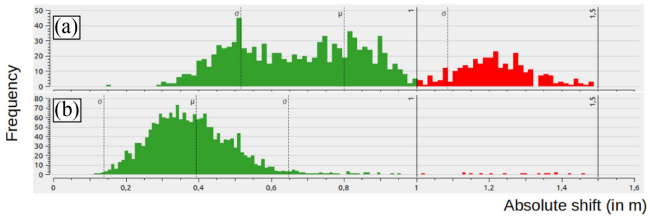

Fig. 6. Recorded histogram of absolute shift errors detected by AROSICS [53] between two VNIR flight-lines acquisitions of 1-day interval before (a) and after (b) the coregistration correction, respectively.

To reduce this geolocation error, an additional registration operation was conducted on all the acquired flight lines.

This coregistration error appears:

1) between acquisitions;
2) between the SWIR and the VNIR sensors (intersensor offset).

This interacquisition and intersensor offset can arise from various sources and uncertainties in the PARGE projection process (see Section II-B2). For each site, all flight lines of all VNIR and SWIR acquisitions (see Section II-B) were coregistered to a common orthorectified mosaic produced from the NIR Phaseone camera. The images used were taken on the first flight date on each site. The coregistration was conducted using AROSICS [53] (see Appendix A). The residual coregistration error between overlapping corrected flight lines was then also estimated with AROSICS [53].

Errors between flight lines were similar whether they were acquired on the same day or not, and each tie point estimation of coregistration error was stored in a dictionary for the Nouragues and Paracou area.

Coregistration accuracy of SWIR and VNIR acquisition differed slightly (the mean distance in pixels between identical pixels from different flight lines was 0.4 pixel for the VNIR and 0.1 pixel for the SWIR, respectively).

4) Metadata of Condition of Acquisition: For each pixel of every flight line, the following metadata was recovered.

1) Sensor viewing angles Azimuth and zenith viewing angles were converted into raster format and incorporated into the VNIR product prior to the coregistration process (see Section II-B3). While minor artifacts may still be visible at the center of each flight line due to the warping process of coregistration correction, we consider these effects to be negligible.
2) Solar angles, initially written in the descriptive flight-line metadata supplied by Hytech-Imaging, azimuth, and zenith solar angles were recovered and integrated during the coacquisition dataset construction (see Section II-C).
3) Illumination coefficient (ILU), the indicator is calculated over a radiometric estimation of the shadow fraction of the pixel [52]. This coefficient is then clipped between 0 and 1 as a proxy for the percentage of direct illumination (see Fig. 7).

5) Coacquisition Dataset: To retrieve common pixels captured by different overlapping flight lines, one could search for each *(x,y)* coordinate of the mosaic, the corresponding acquisitions in each flight line, but the search process would be particularly time consuming.

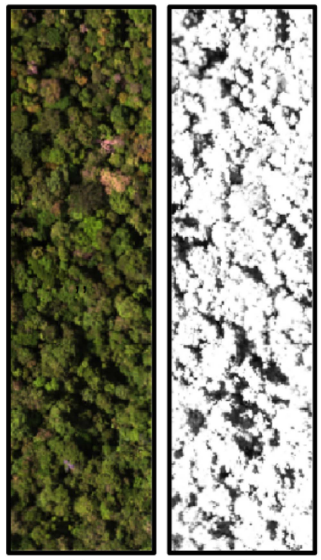

Fig. 7. (a) RGB false color representation of the studied canopy. (b) Illumination coefficient computed over the same area.

All the pixels acquisitions were then regrouped by their coordinates $(X_{\text{mosaic}}, Y_{\text{mosaic}})$ in the NIR mosaic, defining a set E of all possible available coacquisitions for each pixel. This subset E is then later called *coacquisitions* in our study, as it contains all hyperspectral acquisitions of a same location of the DSM mosaic.

C. Spectral Coherence

Coacquisitions were grouped into pairs based on their metadata to study specific sources of variability (see Section II-B5). The general decomposition flow chart is presented in Fig. 8, where each dataset used for this study is the result of specific subsets coming from the general dataset presented.

Only well-illuminated pixels (ILU ≥ 0.95) were considered. In addition, nonforest pixels were carefully masked. These corresponded to water bodies (river in Nouragues), a rocky outcrop (inselberg in Nouragues), various bamboo thickets (in Nouragues), a large clearing (Paracou), and tracks (Paracou) and base camps in both sites. After this data cleansing operation, remaining coacquisitions were paired based on specific differences in their acquisition condition.

The first comparison parameter is the acquisition date, as indicated in Fig. 8.

1) When $\Delta_{\text{Date}} == 0$, there is no change of date between the pairs of acquisition, which defines the intradate dataset. These acquisitions result from overlapping cross-track flight-lines captured the same day.
2) When $\Delta_{\text{Date}} == 1$, there is a change of date of one day between the acquisition pairs, which defines the interdate dataset.

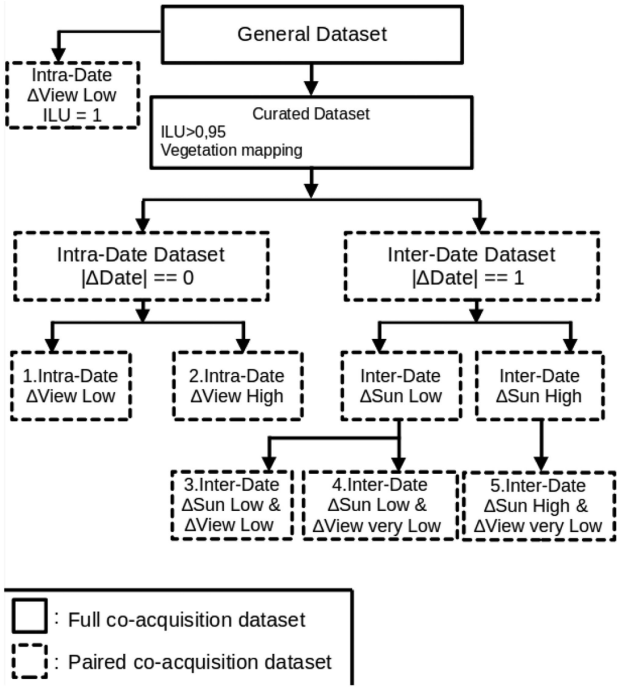

Fig. 8. Flowchart of the different dichotomies implemented for this study.

Other parameters considered when pairing pixels were the difference in viewing and sun angle geometry, respectively corresponding to Δ_{View} and Δ_{Sun}.

Angle variation between acquisitions refers to the relative angle between sun or viewing vectors in the two acquisitions.

To explore the influence of viewing angle variations between a pair of coacquisition (see Section II-C), a first decomposition of the intradate subdatasets is implemented, based on whether pairs exhibit a high or low Δ_{View}.

Pixels from neighboring flight-lines on the same date share identical solar angle and atmospheric conditions, though their Δ_{View} differs from 0 due to the cross-track FOV. This assumption is reexamined in Section II-D.

The opposed flight plans direction over the Nouragues area between dates (see Fig. 4) results in significant Δ_{Sun} variability for interdate coacquisitions (see Fig. 4). In contrast, in the Paracou area, interdate coacquisitions exhibit a low Δ_{Sun} variability due to identical flight plan direction across dates (see Fig. 5).

This allows for decomposition into subdatasets showing coacquisitions with high and low Δ_{Sun} in Nouragues, unlike Paracou (see Fig. 8).

Finally, to meaningfully compare responses across sites, we reduced the discrepancy in solar illumination geometry between the two study sites by restricting the solar zenith range of the Nouragues acquisitions to $[33, 45°]$. This constraint was relaxed to study the influence of Δ_{Sun} for the Nouragues area.

A description of registered variability and the number of coacquisition pairs screened for each dataset presented in Fig. 8 is provided in Tables II and III for Nouragues and Paracou.

From these different subdatasets, it is possible to apply different metrics expressing the amplitude of a spectral variability

TABLE II
DESCRIPTION OF SUBDATASETS OF PAIRED COACQUISITION USED FOR THIS STUDY OVER THE NOURAGUES AREA

Dataset Name	Δ_{View} Variability	Δ_{Sun} Variability	Change in Atmospheric State	Number of pixels	Solar zenith angle
ILU =1 1.Intra-Date Δ_{View} Low	[10°, 12.5°]	None	False	16615	[33°, 45°]
1.Intra-Date Δ_{View} Low	[10°, 12.5°]	None	False	17238	[33°, 45°]
2.Intra-Date Δ_{View} High	[15°, 17.5°]	None	False	95706	[33°, 45°]
3.Inter-Date Δ_{Sun} Very Low & Δ_{View} Low	[10°, 12.5°]	[0°, 5°]	True	17408	[33°, 45°]
4.Inter-Date Δ_{Sun} Low & Δ_{View} very Low	[0°, 5°]	[0°, 10°]	True	76678	[33°, 65°]
5.Inter-Date Δ_{Sun} High & Δ_{View} very Low	[0°, 5°]	[15°, 25°]	True	135827	[33°, 65°]

TABLE III
DESCRIPTION OF SUBDATASETS OF PAIRED COACQUISITION USED FOR THIS STUDY OVER THE PARACOU AREA

Dataset Name	Δ_{View} Variability	Δ_{Sun} Variability	Change in Atmospheric State	Number of contained pixels	Solar zenith angle
ILU = 1 Intra-Date Δ_{View} Low	[10°, 12.5°]	None	False	8341	[15°, 38°]
1.Intra-Date Δ_{View} Low	[10°, 12.5°]	None	False	49990	[15°, 38°]
2.Intra-Date Δ_{View} High	[15°, 17.5°]	None	False	48591	[15°, 38°]
3.Inter-Date Δ_{Sun} High & Δ_{View} Low	[10°, 12.5°]	[12°, 17.5°]	True	47039	[15°, 38°]

(see Sections II-C1, II-C2, and II-C3). The comparison of these metrics between the different subdatasets can then be interpreted as the contribution of each source of variability mentioned above and is presented in Section II-D.

1) Correlation Per Band: Given a dataset of paired acquisitions, spectral variability per band is evaluated using Pearson correlation coefficient between corresponding bands of the paired datasets. This provides a measure of similarity between coacquisitions for each band of the hyperspectral signal.

Several cases of saturation occurred in the SWIR2 domain, see Section II-C2, where vegetation pixels showed more than 20% reflectance. Such spurious values were removed in the SWIR2 domain as they are implausible for vegetation pixels [11]. A bootstrapping operation [54] was implemented for each estimation of the correlation per band, with 200 iterations of the considered dataset for this estimation.

2) Explained Variance: To summarize and present straightforward results on spectral instabilities within a given spectral domain, the mean explained variance is computed based on the correlation per band calculated in Section II-C1.

Spectral acquisition is decomposed into five different spectral domains.

1) VNIR: Corresponds to the Hyspex VNIR camera, covering [414–993 nm].
2) SWIR0: Before the first atmospheric absorption band, covering [977–1330 nm].
3) SWIR1: Between the two atmospheric absorption region, covering [1498–1775 nm].

TABLE IV
SPECTRAL INDEX DEFINITION TABLE

Index	Formula	Sensibility	Author
NDVI	$(R_{800}–R_{670})/(R_{800}+R_{670})$	Photosynthetic Activity	[42], [43], [44]
CHL	$(\frac{1}{R_{540-560}}-\frac{1}{R_{760-800}}).R_{760-800}$	Relative Content of Chlorophyll	[45], [46]
CAR	$(\frac{1}{R_{510-520}}-\frac{1}{R_{690-710}}).R_{760-800}$	Leaf Carotenoids	[45], [46]
EWT	$(1-R_{1,193})/R_{1,126}$	Leaf Water Content	[45], [47]

4) SWIR2: After the last atmospheric absorption region, covering [1981–2361 nm].
5) The entire spectral domain provides a general expression of the recorded spectral coherence across one dataset.

For each spectral domain and paired coacquisition datasets outlined in Section II-C1, the mean correlation within the spectral domain is computed and squared to derive the explained variance of one coacquisition by the other

$$ExplainedVariance = \mu(PersonR_{Bands}[Domain]^2). \quad (1)$$

The result of (1) then provides information about the general stability of the domain spectrum in different domains, or different conditions of acquisition. A bootstrapping was also implemented for each estimation with 200 different iterations of the considered dataset.

3) Spectral Index Coherence: Many vegetation indices can be derived from hyperspectral data, [24], [43], [44], [45]. Some indices are considered to be closely related to particular constituents or structural properties of tree crowns [24], [43], [44], [45]. Indices are also used as first-level embedded spectral attributes to extract physically interpretable values or to later feed into more complex models.

Vegetation indices combining bands in a nonlinear fashion may show a different level of consistency than spectral values. Here, we examine a selection of indices responsive to leaf pigments and water content. These indices are the NDVI, the CHL, the CAR, and the EWT index. Their sensitivity and formula are summarized in Table IV. Since the maximum time between successive flights is 24 hours, this study assumes that chemical and structural properties remained unchanged during data collection.

The variability of each index presented in Table IV is then evaluated by estimating the percentage of explained variance, as shown in (1), of each computed index using the paired coacquisition dataset presented in Section II-C1.

That way, the similarity and robustness of each index can be assessed for different contexts of coacquisition (see Section II-C1).

In the same way as for bands in the SWIR2 domain (see Section II-C1), a few pixels indicating a CHL index not in [0,10] or CAR index not in [0,11] and NDVI index not in [0,1] [55] were filtered out.

4) Coregistration Influence: Despite efforts to achieve subpixel precision, a residual error will persist even after local coregistration with AROSICS [53] (see Fig. 6 in Section II-B3).

We examined the impact of coregistration uncertainty by duplicating a flight line, gradually shifting the duplicated flight line, and analyzing spectral consistency with the reference flight line

$$\forall(i,j) \in [N_{\text{Rows}}, N_{\text{Cols}}], Im_{\text{shifted}}[i,j] = fraction \times Im[i \pm 1, j \pm 1] + (1 - fraction) \times Im[i,j] \quad (2)$$

where Im is the chosen flight line for our study, $Im[i \pm 1, j \pm 1]$ is a random neighboring pixel of $Im[i,j]$ and $fraction$ is the value of the subpixel coregistration error estimated for Im_{shifted}.

This was conducted for both VNIR and SWIR images, each at their native resolution of 1 m GSD and 2 m GSD, respectively (see Section II-B). Thus, a 0.5 pixel error corresponds to 0.5 m GSD and 1 GSD for VNIR and SWIR images. The spectrum of each pixel of the shifted flight line was estimated using (2). Spectra pairs extracted formed a paired coacquisition dataset (see Section II-C1).

For various $fraction$ values, the correlation per band between the estimated shifted flight line spectrum $Im_{shifted}$ and the reference Im is evaluated, as detailed in Section II-C1. We report the percentage of explained variance of $Im_{shifted}$ by Im for $fraction$ values ranging from 0.1 to 0.9 pixel coregistration error for different spectral domains (see Section II-C2). The explained variance is given per spectral domain in Table XI (see Section II-C2). Fixed values of $fraction$ were used to provide an order of magnitude of misregistration impact, aiding the discussion on its influence on spectral variability (see Section IV-B1). Additionally, a plot representing the correlation per band was generated, mimicking actual estimated misregistration values rather than fixed ones, as observed in this study. The coregistration error was simulated by replicating the observed geolocation uncertainty across coregistered flight lines (Section II-B3).

D. Influence of Sources of Variability

Concerning single date coacquisitions, as two successive flight lines of the same date are acquired 2 to 4 min apart, the Δ_{Sun} and the atmospheric state can be considered as stable, be it AOT [56], [57] or water vapor content [58]. Using single date acquisitions, it is then possible to highlight the influence of illumination and viewing angle.

1) By comparing the spectral coherence, between low Δ_{View} where $ILU \in [0.95, 1]$ and the same Δ_{View} conditions but where $ILU = 1$.
2) By comparing the spectral coherence between low Δ_{View} and high Δ_{View}.

Concerning mixed date coacquisitions, differences in atmospheric conditions between days, detailed in Section II-B2, allow us to assess their impact by contrasting spectral coherence within intradate datasets with low Δ_{View} to interdate datasets exhibiting the same low Δ_{View} and low Δ_{Sun}. The Nouragues

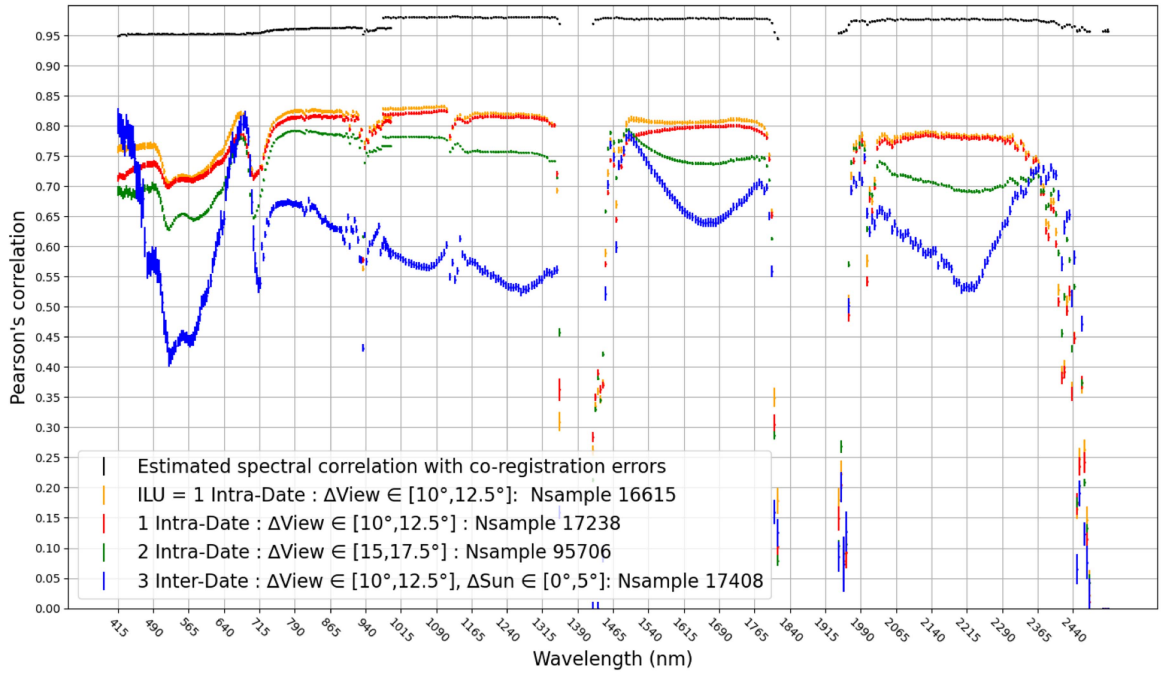

Fig. 9. Band correlation between acquisitions across subdatasets presented in Section II-C for the Nouragues area.

site, characterized by opposing flight directions between dates, facilitates the recording of coacquisitions with minimal solar angle variation, enabling the generation of subdatasets with low or no Δ_{Sun} variability. In contrast, in the Paracou site, consistent flight direction but varying acquisition times result in relatively constant registered Δ_{Sun} within a range of 12° to 17.5° (see Table III, between acquisitions, making it impossible to separate the influence of solar angle and atmospheric state when comparing dates.

Thus, only in the Nouragues area, comparing spectral coherence metrics between interdate datasets with low and high Δ_{Sun} while maintaining low Δ_{View} emphasizes solar angle influence under varying atmospheric conditions.

Concerning neglected factors that affect repeatability, unregistered sources of variability may affect the spectral consistency between different images. The loss of spectral consistency between two near-identical replications was evaluated by comparing the closest acquisition pairs (ILU coefficient of 1 with low Δ_{View}) on each site (see Tables II and III).

While this study accounts for ILU threshold changes in subdataset creation, it does not address substantial alterations in illumination, such as shadows from nearby canopies or clouds [52]. Our focus is on minor variations in ILU values, analyzing if ILU values of 0.95 still represent well-illuminated pixels compared to pixels showing ILU values of 1. We do not examine significant changes in illumination conditions, like shadows or cloud cast shadows, which result in very low ILU coefficients.

The influence of adjacency effects, topography, canopy structure, and surface shape on spectral variability was considered constant across repeated acquisitions.

A bootstrapping operation with 200 iterations was implemented to evaluate the uncertainty level of the spectral correlation, Figs. 9, 10, and the explained variance by spectral range (see Tables XIV and XV, respectively, for the Nouragues and Paracou area.

For the estimation of spectral coherence, we did not bootstrap an estimate of the variability of the coregistration error as is effect was negligible Figs. 9 and 10.

Table V summarizes which subdatasets are compared to express the influence of a given source of variability.

The sources of variability considered for each study site and spectral product are presented in Table VI.

Results are presented for each subdataset in Appendix B, reporting coherence of full spectra or coherence of spectral indices. These are then compared with each other and their relative influence on variability is discussed in Section IV.

III. Results

A. Correlation Per Bands

As indicated in Section II-C, the correlation per band, is computed over each subdataset presented in Section II-C and plotted in Fig. 9 for the Nouragues area and in Fig. 10 for the Paracou area. Specific characteristics of each subdataset is recalled in each label of plotted correlation per band but is also presented in Tables II and III for the Nouragues and Paracou area, respectively.

In figures (see Figs. 9–11), the vertical bars show twice the bootstrapped standard deviation centered around the mean.

Additionally, as the Nouragues site showed greater variability in solar angles (up to 65%), it was possible to study the influence of large and small variability in solar angles between acquisitions, represented by subdatasets N°4 and N°5 (see Table II). Correlation per band over of these subdatasets and their

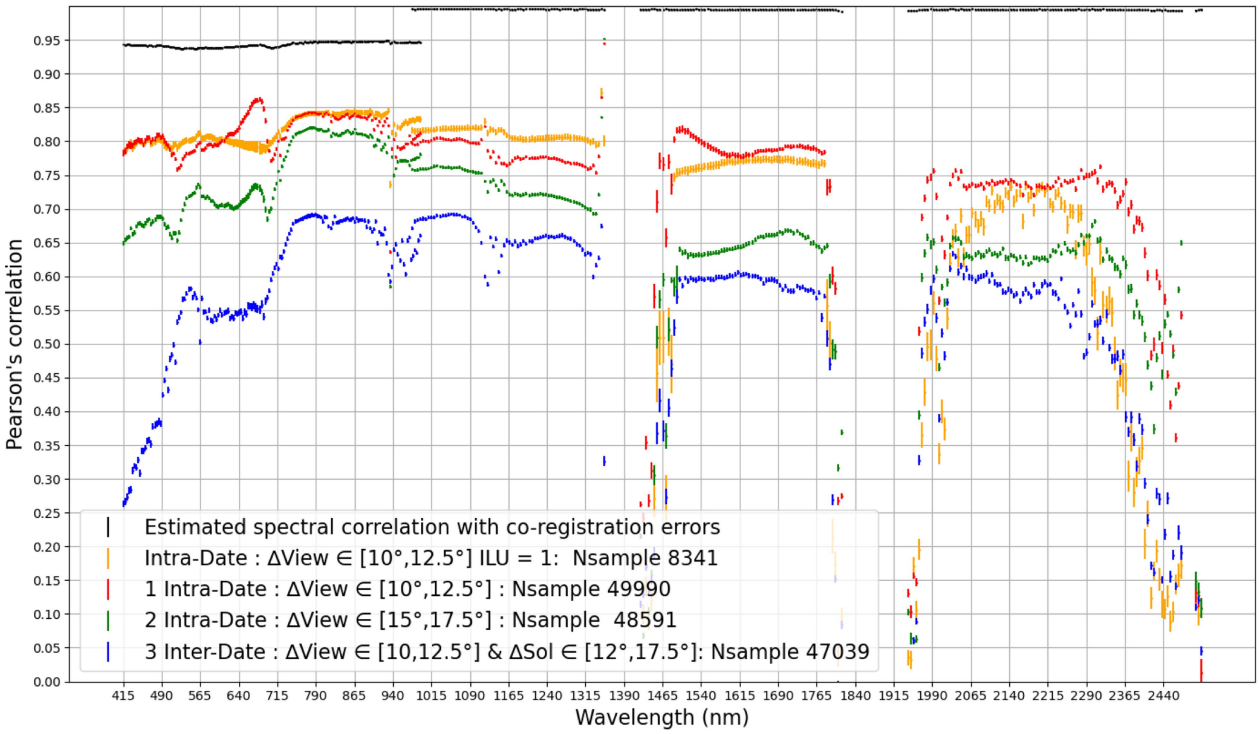

Fig. 10. Band correlation between acquisitions over subdatasets presented in Section II-C for the Paracou area.

TABLE V
COMPARISON TABLE EXPRESSING THE INFLUENCE OF SOURCES OF VARIABILITY OVER SPECTRAL VARIABILITY

Dataset name	Compared dataset name	Expressed source of variability
Coregistration error estimation	ILU = 1, Intra-Date, Δ_{View} Low	Unknown sources
ILU = 1, Intra-Date, Δ_{View} Low	1.Intra-Date Δ_{View} Low	Illumination conditions
1.Intra-Date Δ_{View} Low	2.Intra-Date Δ_{View} High	Viewing Angle
1.Intra-Date Δ_{View} Low	3.Inter-Date Δ_{Sun} Low & Δ_{View} Low	Atmospheric State
4.Inter-Date Δ_{Sun} Low & Δ_{View} very Low	5.Inter-Date Δ_{Sun} High & Δ_{View} very Low	Sun Angle & Atmospheric state

corresponding explained variance per spectral domains are presented in Fig. 11 and Table XIV.

B. Influence of Sources of Variability

Detailed results per subdataset are presented in the appendix (Section B) and regroup the recorded explained variance between pairs of acquisition across subdataset per spectral domains (see Section II-C2) and for spectral indexes (see Section II-C3).

The influences of the various sources of variability per spectral domain are presented in Tables VII and VIII for the Nouragues and Paracou area, respectively. In this table, we report the drop in the coefficient of determination of the relation between one acquisition and another contrasting a particular factor. When uncertainty reaches 1 point, it is reported as $\pm 2\sigma$, where σ is estimated by bootstrap.

Influence of sources of variability given spectral indexes is presented in Tables IX and X, respectively, for the Nouragues and Paracou area.

Additionally, the influence of different values of coregistration error amplitude, utilizing synthetic data as a reference point, is presented results in Table XI. These data provide insight into the drop in explained variance that might be expected in the different spectral domains (see Section II-C2) for a given coregistration error.

IV. DISCUSSION

A. Influence of Major Sources of Variability

1) Influence of Viewing Angles: Comparing intradate datasets with high and low Δ_{View} provides insight into the impact of viewing angle difference (see Table V). The loss of explained

TABLE VI
HIGHLIGHTED SOURCES OF VARIABILITY GIVEN STUDY AREAS AND CONSIDERED PRODUCT

Sources of variability	Nouragues Spectral Coherence	Paracou Spectral Coherence	Nouragues Index Coherence	Paracou Index Coherence
Unknown sources	✓	✓	✗	✗
Illumination conditions	✓	✓	✗	✗
Viewing Angle	✓	✓	✓	✓
Atmospheric State	✓	✗	✓	✓
Sun Angle & Atmospheric state	✓	✓	✓	✗

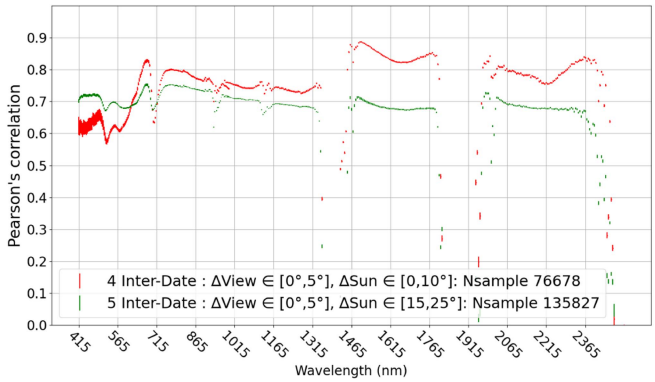

Fig. 11. Band correlation between acquisitions over subdatasets presented in Section II-C for the Nouragues area.

TABLE VII
INFLUENCE OF SOURCES OF VARIABILITY ON SPECTRAL COHERENCE FOR DIFFERENT SPECTRAL DOMAINS OVER THE NOURAGUES AREA

	VNIR	SWIR0	SWIR1	SWIR2	All Spectra
Viewing angles	5%	7%	5%	4% ± 1%	5%
Illumination	2%	1%	2%	1%	2%
Atmospheric state	19%	34%	13%	12% ± 1%	19%
Sun angles & atmospheric state	1%	8%	25%	18%	11%
Unexplained sources	38%	37%	42%	52%	42%

TABLE VIII
INFLUENCE OF SOURCES OF VARIABILITY ON SPECTRAL COHERENCE FOR DIFFERENT SPECTRAL DOMAINS OVER THE PARACOU AREA

	VNIR	SWIR0	SWIR1	SWIR2	All Spectra
Viewing angles	10%	7%	19%	11%	12%
Illumination	1%	4%	-8%	-15%	-4%
Sun angles & atmospheric state	32%	19%	27%	21%	26%
Unexplained sources	22%	33%	52%	68%	41%

TABLE IX
RECORDED DROP OF EXPLAINED VARIANCE OVER DIFFERENT SPECTRAL INDEX GIVEN DIFFERENT IDENTIFIED SOURCES OF VARIABILITY OVER THE PARACOU AREA

	NDVI	CHL	CAR	EWT
Viewing Angles	7%±1%	5%±1%	4%±1%	4%±1%
Sun Angles & Atmospheric State	30%±1%	40%±1%	25%±1%	43%±1%

TABLE X
RECORDED DROP OF EXPLAINED VARIANCE OVER DIFFERENT SPECTRAL INDEX GIVEN DIFFERENT IDENTIFIED SOURCES OF VARIABILITY OVER THE NOURAGUES AREA

	NDVI	CHL	CAR	EWT
Viewing angles	-7%±1%	1%±1%	-25%±1%	5%±2%
Atmospheric state	-11%±1%	-5%±1%	-13%±2%	7%±2%
Sun angles & atmospheric state	7%	19%±1%	54%±1%	14%±1%

TABLE XI
PERCENTAGE EXPLANATION OF VARIABILITY IN EACH DOMAIN FOR DIFFERENT TYPES OF COREGISTRATION ERRORS

Explained Variance / fraction	0.9	0.7	0.4	0.1
VNIR	64%	77%	92%	100%
SWIR0	58%	73%	91%	99%
SWIR1	53%	69%	90%	99%
SWIR2	45%	63%	88%	99%
All Spectra	56%	71%	90%	99%

variance due to viewing angle difference is 5 points and 12 points for the Nouragues and Paracou sites, respectively (see Tables VII and VIII). Although more pronounced in Paracou, this influence remains relatively consistent across spectral domains. However, bands from 415 to 700 nm in the VNIR domain are more affected by viewing angle variability than those in the SWIR1 and SWIR2 domains, as indicated by the correlation analysis (see Figs. 9 and 10).

For the Nouragues site, NDVI and CAR indices exhibit greater consistency in datasets with high angular variability (see Table X). Conversely, all indices in Paracou show reduced coherence (see Fig. 10). However, the influence of viewing angles on indices is weaker than on spectral domains, as evidenced by the EWT and CHL coherence loss across both sites and all indices in Paracou. Vögtli et al. [36] observed similar trends, also noting that while general albedo became more robust to viewing angle after BRDF correction, NDVI did not, likely due to the nonlinear nature of index computations.

2) Influence of Atmospheric State: The time difference between dataset n°1 and n°3 introduces variations in atmospheric conditions, impacting the explained variance (see Table II). In Nouragues, flying lines starting from opposite end on the two dates led to low solar angle variability at the center of the study area, whereas Paracou flight lines consistently exhibited sun-angle differences exceeding 10° from one another due to temporal shifts in the flight plan, see Section II-D. Consequently,

the analysis of atmospheric influence in Paracou remains conditional on sun angle variability.

Focusing on Nouragues (see Fig. 9) the correlation decline between datasets n°1 and n°3 primarily impacts the [490 nm, 640 nm] region, with negligible effects observed within the [640 nm, 715 nm] range, gradually worsening toward the SWIR1 range. Overall, atmospheric variations emerge as the predominant source of spectral instability, resulting in a 19% and up to 34% decrease in explained variance in the VNIR and SWIR0 domains, see Table VII, respectively. Further, it is to be noted that constant aerosol amounts have been assumed per day for the correction. The influence of the atmosphere then appears to decrease in the SWIR1 and SWIR2 domain.

The influence of the atmospheric state on the spectral indices was assessed by comparing the explained variance of each computed pair of the dataset n°1 to the dataset n°3 (see Table X). The unexpected increase (negative drop) in explained coherence for the NDVI and CAR index could be due to some of their bands being located in the [640 nm,715 nm] area, which is not the case for the CHL index. Overall, spectral indices seem less sensitive to the influence of a date change than spectral bands.

3) Influence of Solar Angle & Atmospheric State: To assess the impact of solar angle variability in Nouragues, contrasting interdate datasets (n°4 with low solar angle difference and n°5 with high solar angle difference) revealed higher coherence compared to dataset n°3 (see Table II, Fig. 9, and Fig. 11). Datasets n°4 and n°5 incorporated acquisitions with zenith solar angles exceeding 60°, deviating from the 33° to 45° range used elsewhere to mimic Paracou's solar conditions.

This relaxation likely introduced a different canopy illumination context, explaining the increased coherence. Solar angle's influence, highlighted in Table VII, emerges as the second most significant variability source, particularly in SWIR1 and SWIR2, diminishing in SWIR0, and minimal in VNIR (see Table X). It induces a loss of explained variance of 1% in VNIR, 8% in SWIR0, 25% in SWIR1, and 18% in SWIR2 domain (see Table X), accounting for an 11% loss across the spectrum.

In the [415 nm, 630 nm] region, larger solar angle differences resulted in greater coherence, possibly influenced by AOT (see Table II). This suggests a more dominant atmospheric influence due to lower vegetation reflectance in this region [11], [19], [24].

The flight paths of Nouragues from opposing starting points for the same trajectory imply that central area acquisitions had the closest time of day, unlike those further east or west. Coacquisitions with low solar angle variation likely came from central flight lines, while high variability acquisitions were from off-centered areas (see Section II-B1). The coherence gain of dataset n°5 in the [415nm–500nm] range compared to n°4 could be attributed to spatial variability in aerosols across the study area. Such effects might be significant if slight haze conditions were present in the data, considering that the correction did not account for spatial variations of aerosols (see Table II).

Canopy scattering, influenced by leaf orientation variations also impacts spectral variability, notably after the red-edge area. Solar angle variations may further affect scattering effects as different solar angles induce different scattering paths [11], [19], [24].

A large difference in sun angle during acquisition also means varying times of day for data collection, potentially introducing diurnal sources of variability, including evapotranspiration regime affecting the lower atmosphere and other atmospheric changes, which may impact the spectrum [59], [60].

The combined impact of interdate atmospheric and solar angle differences on spectral indices was evaluated by comparing explained variance loss between datasets n°4 and n°5 (see Tables V and X). Solar angle influences reduced NDVI, CHL, CAR, and EWT explained variance by 7%, 19%, 54%, and 14%, respectively. To this extent, solar angle variability seems to be the most important source of variability affecting spectral indices.

The Paracou analysis involves comparing intradate datasets with low Δ_{View} (10°–12.5°) to interdate datasets with Δ_{View} in the same range and Δ_{Sun} from 12° to 17.5°. Integrating solar and atmospheric variability yields the most significant source of variability in Paracou, reducing the overall explained variance by 26% across the spectral range (see Table VIII).

Specific spectral domains impacted include a 27% drop in SWIR1 and 32% in VNIR explained variance, mainly concentrated in the [415nm, 715nm] visible range. For indices, joint atmospheric and viewing angle influence decreases NDVI, CHL, CAR, and EWT explained variances by 30%, 40%, 25%, and 43%, respectively.

Initially, juxtaposing two datasets with significantly varying acquisition (atmospheric and solar angle variability) conditions between pairs might appear as an irrelevant approach to illustrate hyperspectral acquisition sensitivity for each of those sources of variability. However, it is important to acknowledge that this comparison essentially equates to contrasting a standard overflight of an area, characterized by a slight disparity in acquisition time and adherence to the same overflight plan.

4) Unregistered Sources of Variability: The decrease in explained variance not ascribable to coregistration errors V, varies across the entire spectral domain see Figs. 9 and 10. The average decrease also differs between different spectral regions (see Tables VII and VIII).

The SWIR domain contains bands much affected by the atmosphere absorption between 1350 to 1465 nm and between 1900 and 1950 nm, i.e., in strong water vapor absorbance regions. A cross-talk between inaccurate modeling of atmospheric scattering due to missing aerosol information and water vapor absorption can amplify this effect. In the SWIR2, the drop in sensitivity of the spectral sensor above 2380 nm can also impact the overall explained variance in this domain. A slight drop in coherence around 940 nm may result from the junction of the VNIR and SWIR sensors (see Section II-B) and their reduced sensitivity in this spectral region, compounded by highly variable atmospheric compensation, leading to potential instability.

In the VNIR domain, the drop of coherence in the red-edge region from 675 to 752 nm known to be a transitioning spectral region between high reflectance bands in the NIR due to a scattering phenomenon [24] is quite clear. The visible domain, in which vegetation reflectance is low, appears to be the most unstable region overall, especially in the green. The fairly low coherence in the 490 to 640 nm region could be related to the variability of viewing angles as the light trajectory through the

TABLE XII
DESCRIPTION OF THE SPECTRAL RANGE DEFINED TO BUILD NIR PROXIES FOR VNIR AND SWIR PRODUCTS

NIR Proxy / Sensor	VNIR	SWIR
Wavelength λ (nm)	949.5–993.2	976.8–1004.0

TABLE XIII
HYPERPARAMETERS USED FOR LOCAL AROSICS IMPLEMENTATION

	Band Match	grid res	Window size	Min reliability	Max Shift	Align grids	Match GSD
VNIR	Proxy VNIR	16	(32,32)	0	8	True	True
SWIR	Proxy SWIR	8	(16,16)	0	8	True	True

TABLE XIV
PERCENTAGE OF EXPLANATION OF VARIABILITY FOR EACH SPECTRAL DOMAIN OVER SUBDATASETS PRESENTED IN SECTION II-C OVER THE NOURAGUES AREA

Subdataset	VNIR	SWIR0	SWIR1	SWIR2	All Spectra
Coregistration Influence	89%	99%	99%	99%	95%
ILU = 1 Intradate Δ_{View} Low	67%	66%	47%	31%	54%
1. Intradate Δ_{View} Low	66%	62%	55%	46%	58%
2. Intradate Δ_{View} High	56%	55%	36%	34%	47%
3. Intradate Δ_{View} Low $\Delta_{Sol} \in$ [12°,17.5°]	34%	43%	28%	24%	32%

canopy is modified, resulting in a varying expression of leaves pigments and less coherence across this spectral area [24].

Finally, it is worth noting a systematic dip in correlation at 900 nm, likely resulting from imperfect atmospheric compensation of water absorption.

In addition to specific bands, Figs. 9 and 10 show a significant overall coherence loss, likely due to varying viewing angles, calibration, and atmospheric correction, as noted by [36].

Beyond coregistration errors, other sources of variability should be considered. The potential impacts of spectral smile, keystone effects, rotation effects, and striping [61], [62] were evaluated on an internal study and were found negligible.

Spectral calibration techniques, [63], [64], could have been useful in further reducing the spectral variability in our data. However, in the tropical rainforest environment, it was not feasible to implement this calibration due to the absence of appropriate reference surfaces. Without suitable and well-illuminated openings in the rainforest canopy, in situ spectral calibration was not possible.

As a result, the lack of calibration could contribute to the unregistered variability in our results.

B. Influence of Proxies of Sources of Variability

1) Influence of Coregistration: Figs. 9, 10 and Tables XIV and XV in the appendix suggest that residual coregistration errors contribute little to the drop in spectral coherence observed in the current study. The largest decrease in explained variance,

TABLE XV
PERCENTAGE OF EXPLANATION OF VARIABILITY FOR EACH SPECTRAL DOMAIN OVER SUBDATASETS PRESENTED IN SECTION II-C OVER THE PARACOU AREA

SubDataset	VNIR	SWIR0	SWIR1	SWIR2	All Spectra
Co-registration Influence	92%	96%	96%	95%	94%
ILU = 1 Intra-Date Δ_{View} Low	61%	66%	58%	48%	58%
1. Intra-Date Δ_{View} Low	58%	65%	56%	47%	56%
2. Intra-Date Δ_{View} High	53%	58%	52%	43%±1%	51%
3. Inter-Date Δ_{View} Low Δ_{Sol} Very Low	40%	31%	43%	36%±1%	38%
4. Inter-Date Δ_{View} Very Low Δ_{Sol} Low	52%	55%	67%	57% ± 1%	57%
5. Inter-Date Δ_{View} Very Low Δ_{Sol} High	51%	47%	42%	39% ± 1%	46%

less than 11% in the VNIR for Paracou acquisitions, is notably smaller than declines observed in the most consistent coacquisitions over Nouragues and Paracou (42% and 46%, respectively).

Results from Table XI emphasize the necessity of precise coregistration before comparing pixel-to-pixel reflectance. Errors exceeding 0.7 pixels (VNIR) and 0.9 pixels (SWIR) lead to coherence reduction akin to variability in Tables VII and VIII. This suggests that beyond these thresholds, the influence of the spatial coregistration surpasses environmental variability. Ensuring accurate coregistration is thus vital for maintaining spectral coherence and reliable pixel-level comparisons.

2) Influence of Illumination Condition: The impact of illumination variability was assessed by comparing highly illuminated (ILU =1) intradate subdatasets with less restrictive illumination coefficients (ILU $\in$ [0.95,1]) (see Table V). In the Nouragues area, illumination had minimal impact, reducing explained variance by 2 points on average across bands and spectral domains (see Table VII). In Paracou, less constrained illumination coefficients resulted in 4 points less explained variance (see Table VIII).

Consequently, the variability within the range [0.95,1] of ILU appeared negligible, justifying the use of a less restrictive threshold (ILU $\geq$ 0.95) for the creation of subdatasets (Section II-C). This decision aligns with the observed behavior and addresses potential limitations in the ILU coefficient's accuracy.

C. Overall Discussion

1) Spectral Coherence: In summary, according to Tables VII and VIII, the atmospheric state seems to be the most important registered source of variability followed by sun angle variation, viewing angle variation, and then illumination condition variation. Thus, quantifying the spatial variability of both the water vapor absorption and the aerosol scattering is crucial in the atmospheric correction process.

The strong impact of the remaining atmospheric perturbations does not come as a surprise. Doxani et al. [65] highlighted the

limitations of pure physical inversion methods in estimating atmospheric parameters, with around 5% accuracy for water vapor retrieval on hyperspectral images [66]. AOT retrieval uncertainty is about 0.1 [65], and surface reflectance accuracy is estimated at 5% relative difference [67]. While these estimates are derived from satellite imagery, they generally apply under more demanding conditions than clear-sky airborne acquisitions. Interdate coacquisitions for atmospheric comparison (see Tables II and V) also introduce sun angle variability, potentially causing uncorrected BRDF effects.

For the SWIR1 and SWIR2 domains, variability of sun angles is the most important source of variability, followed by atmospheric state, viewing angle and illumination condition. The VNIR and SWIR0 follow the same ranking as the overall spectral domain.

2) Vegetation Indices Coherence: Although seemingly more coherent than raw bands, some indices showed significant drops in explained variance, up to 54% between subdatasets (see Table X).

This indicates that although these indices are useful for characterizing physicochemical properties from a vegetation spectrum, these proxies remain sensitive to changes in acquisition conditions that are not related to the nature of the pixel zone that the reflectance should represent, even at the meter scale [36], [68], [69]. This variability could affect the robustness of methods that take into account such vegetation indices [45], [70], and lead to misleading results [71], [72].

Even normalized indices such as NDVI showed a reduction in coherence with changes in viewing angle, indicating complexities that were not mitigated by normalization [36]. This highlights the challenges in interpreting vegetation indices, urging caution in their application for accurate characterization of vegetation properties.

3) Visible Spectral Area: The visible spectral range exhibits high sensitivity to acquisition conditions, likely due to changes in visibility and aerosol optical depth (AOD) during coacquisition [17]. This variability underscores the importance of accurate aerosol correction. Such fluctuation and a lack of proper spatialized AOT correction might explain the significant coherence drops between dataset n°1 and n°3 in both Paracou and Nouragues areas, as observed in Figs. 9 and 10, despite contradictory findings for Nouragues in the [415 nm, 500 nm] domain.

The significant influence is unexpected, considering the recorded AOT levels below 0.2 between dates, classified as low [51] (see Section II-B2). This differs notably from typical AOT in rainforests [73].

D. Limitations

This study relies on different approximations to characterize the differences in acquisition conditions, which almost certainly limited our ability to accurately quantify their effects.

First, the coregistration process with AROSICS [53] involves warping functions to reproject flight lines onto a common geometry, reducing spatial resolution, which adds up to the general spatial uncertainty due to rasterization [74]. Estimation of residual coregistration errors is also an approximation [53], contributing to uncertainty in the $fraction$ value used for the shifted spectrum estimation (2).

Second, the use of the ILU coefficient, central in this study, is a useful oversimplification intended to give a proxy of the direct illumination of an area on the ground. Despite this simplification, this study assumed that only keeping indicators between 0.95 and 1 would imply using pixels unaffected by shadows cast by the canopy or clouds, which remain the primary source of illumination change. Finer variability of illumination could still be represented within pruned subdatasets.

Third, in this study, BRDF effects were analyzed considering solar and viewing angle variability independently, although solar and viewing angle have a strongly related effect [31], [32], [75]. However, because of the complexities arising from their interaction in the present interpretation of the results, mostly concerning the different representation of solar angles between Nouragues and Paracou, this study focuses on the independent influence of viewing and solar angles on the reflectance sensibility.

Finally, considering atmospheric variability as a binary difference between dates warrants reconsideration. Per-pixel quantification per scene is preferable, factoring in calibration and weather nuances such as spatialized AOT [52].

Unstudied interactions with atmospheric correction operations may contribute to the unaccounted variability. Stable registered atmospheric state across dates and low viewing angle variability in the study acquisition may affect reflectance variability assessment as not all use cases were explored. Resolution changes were not explored but could mitigate coregistration errors.

V. Conclusion

A. Conclusion

Repeated acquisitions over a tropical forest canopy, followed by atmospheric correction and coregistration, facilitated the creation of subdatasets focusing on various sources of spectral variability separately. Characterization encompassed bandwise, spectral domain, and spectral index analyses. However, real acquisitions cannot actually fully isolate individual sources of variability, often intertwining with other mechanisms. Fundamentally, the study serves as a sensitivity analysis, exploring an ATCOR4 flat terrain-corrected reflectance and a few derived vegetation indices responses to known sources of variability.

We observed that even under relatively stable atmospheric conditions, the sources of spectral variability could be ranked in decreasing order of importance as follows for the VNIR domain:

1) state of atmosphere;
2) solar angles;
3) viewing angles.

And as follows for the SWIR domain:

1) solar angles;
2) state of atmosphere;
3) viewing angles.

Despite the low variability in atmospheric conditions, we found that it still played a significant role in spectral variability,

suggesting that it may be a major contributing factor to spectral variability.

The influence of the registration error, the illumination conditions as well as the residual unexplained variability were also considered. Although the illumination variations recorded remained very small, their influence was nonnegligible, confirming the importance of this source of variability on the reflectance spectra. The registration error, in the context of a tropical forest at a resolution of 1 m for VNIR and 2 m for SWIR, becomes a major source of variability for an infra-pixel error of 0.7 pixels for VNIR and 0.9 pixels for SWIR, implying that it is essential to reach this coregistration rate to consider pixelwise comparison across acquisitions.

Exploring these methods to assess the influence of environmental spectral variability in airborne hyperspectral acquisitions is expected to offer insights into correcting or integrating such variability in real-world acquisitions, rather than simulated ones.

B. Perspectives

The present study, which characterizes the spectral variability of a product in reflectivity as a function of different sources of abiotic variability, opens-up several perspectives.

One avenue involves advanced diagnostics of spectral variability using radiative transfer simulations on 3-D forest scenes. Experimental studies are inherently limited in exploring few cases across which the various factors affecting the computed reflectance will covary. A complementary study could aim at highlighting the various sources of spectral variability in a controlled environment and exploring more systematically their interactions. The modeling of the canopy structure from high-density LiDAR could inform in silico simulations like DART [32] to better understand hyperspectral signal acquisition mechanisms.

Second, this study clearly shows strong influences of atmospheric conditions after a standard atmospheric correction. Thus, the atmospheric correction process has to be optimized and further improved for application in tropical environments. Strong intraday and interday differences may be present due to local climate conditions, which are to be analyzed based on the imagery. The aerosol optical thickness, but also aerosol type, water vapor amount, and possible cross-talks between humidity and aerosol sizes are to be taken into account to improve the retrieved reflectance values.

Third, while this study focuses on tropical forests, future research should assess whether our findings on atmospheric, solar, and viewing angles apply to other ecosystems. The porous structure of forest canopies limits direct comparisons with other land covers, making it essential to extend similar studies to different environments and atmospheric correction methods.

A final perspective would be to consider these various spectral coherence tests over airborne acquisition as diagnostics and validation operations for potential spectral representations resilient to these sources of variability.

Not only would these different diagnostics help define the resilience of any spectrum representation, they could also define the range of variability of the acquisition conditions, beyond which:

1) either coherence of the recorded representation becomes too low to consider the spectral representation as stable in a given acquisition context;
2) either a dataset is not variable enough to identify whether the spectral representation considered remains coherent.

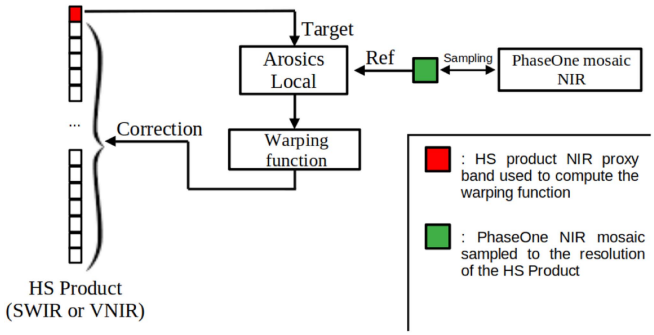

Fig. 12. Flowchart of AROSICS processing.

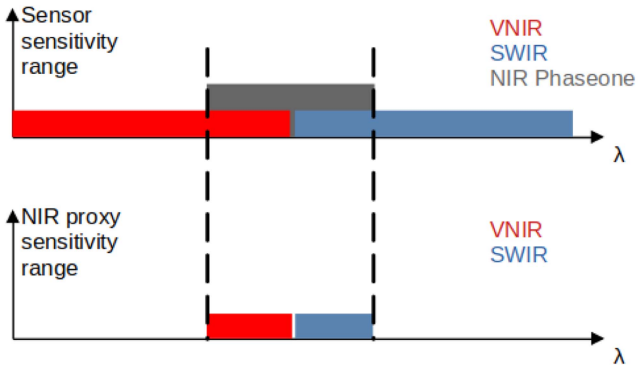

Fig. 13. Choice of VNIR and SWIR bands to produce NIR proxies.

Appendix A
Coregistration Operation

The Arosics software [53] was used to realign all the flight lines for each zone to the same mosaic for VNIR and SWIR, using a mosaic constructed from the NIR PhaseOne camera acquisitions (see Section II-B).

The advantage of the NIR spectral range is that it encompasses spectral bands present in both VNIR and SWIR acquisitions. Unfortunately, the spectral range sensitivity of the phase one camera, IXA-R 160, has not been communicated, so the choice of bands used to produce the NIR proxy for the VNIR and SWIR products was based on the definition of the NIR spectral range.

As indicated in Fig. 12, for each flight line and for each sensor, a proxy of the NIR reflectance of the flight line is estimated across the bands, so that it correlates best with the reflectance information in the NIR mosaic (see Fig. 13).

Finally, to calculate this NIR proxy, for each sensor, we averaged the bands described in the interval presented in Table XII to finally produce the reference band used by AROSICS to

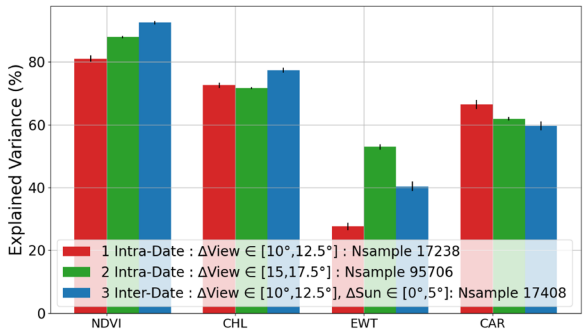

Fig. 14. Percentage of explanation of variability for each spectral index over subdatasets presented in Section II-C over the Nouragues area.

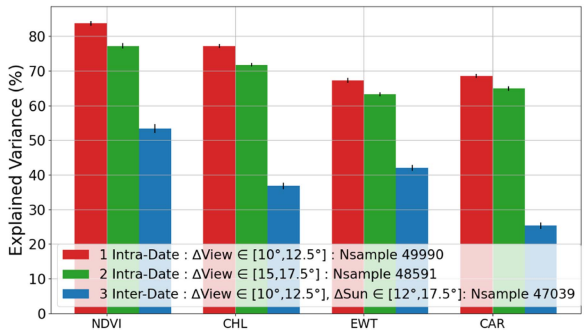

Fig. 15. Percentage of explanation of variability for each spectral index over subdatasets presented in Section II-C over the Paracou area.

calculate the warping function that will apply to all the rest of the product's bands.

The Arosics software can be used in "local" mode. Such approach involves warping the raster based on calculated phase shifts per snap point, often requiring bilinear interpolation and leading to resolution/contrast loss. Hyperparameters in Table XIII are chosen to map coregistration functions detecting spatial patterns between SWIR and VNIR products. Grid resolution and window size are determined by SWIR and VNIR resolutions during coregistration, aiming to map a 32 m estimation window for both. The minimum reliability of 0 disregards the indicator's dependency on window size, prioritizing correction of refined-scale coregistration errors. The *Max Shift* value, less critical due to the expected global one-pixel registration error, mainly restrains tie point computation output using SSIM and RANSAC criteria. *Align grids* and *match gsd* parameters reproject flight lines onto the reference geo-grid to a 1 m (GSD) resolution.

Appendix B
Results Per Subdatasets

Tables presenting explained variance between pairs of acquisition per subdataset, presented in Section II-C in Table II for the Nouragues area and Table III for the Paracou area, accross spectral domains, are presented in Tables XIV and XV, respectively, for the Nouragues and Paracou. Recorded incertitude interval defined as $\pm 2 * \sigma$, where σ is the estimated standard deviation from the bootstrapped estimations, the percentage precision was not integrated in the presented table.

Additionally, figures of recorded explained variance between computed pairs of spectral indexes between subdatasets as presented in Section II-C3 are provided in this appendix. Figs. 14 and 15 illustrate the recorded explained variance for the subdatasets likely in common between the Nouragues and Paracou. The variability of explained variance estimation is observed through bootstrapping and depicted in Figs. 14–16. In these figures, the black bars represent twice the standard deviation estimated from the bootstrap operation, centered around the mean of the various bootstrap iterations.

As more solar angle variability was recorded in the Nouragues acquisitions (see Table II) subdatasets illustrating solar angle variability were constructed and the explained variance between pairs of spectral indexes over those datasets is illustrated in Fig. 16.

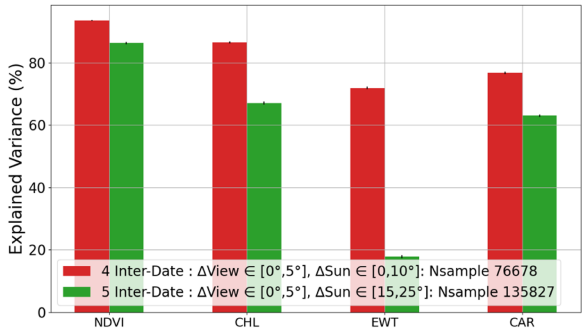

Fig. 16. Percentage of explanation of variability for each spectral index across subdatasets N°4 and N°5 presented in Section II-C over the Nouragues area.

Acknowledgment

The authors would like to thank the Institut des Mathématiques pour la Planéte Terre (IMPT) foundation, Centre national d'études spatiales (CNES), and Hytech-Imaging for the airborne imaging data and also the laboratory of excellence CEBA (Center for the Study of Biodiversity in Amazonia, "Investissement d'Avenir" programs managed by Agence Nationale de la Recherche [CEBA, ref. ANR-10-LABX-25-01]) for the support of the research team. Authors declare no conflict of interest. Artificial intelligence systems were used to improve grammar and readability.

References

[1] A. Esquivel-Muelbert et al., "Compositional response of amazon forests to climate change," *Glob. Change Biol.*, vol. 25, no. 1, pp. 39–56, 2019.
[2] A. C. Roosevelt, "The amazon and the anthropocene: 13,000 years of human influence in a tropical rainforest," *Anthropocene*, vol. 4, pp. 69–87, 2013.
[3] W. F. Laurance, M. Goosem, and S. G. Laurance, "Impacts of roads and linear clearings on tropical forests," *Trends Ecol. Evol.*, vol. 24, no. 12, pp. 659–669, 2009.
[4] S. E. Ahmed et al., "Road networks predict human influence on amazonian bird communities," *Proc. Roy. Soc. B: Biol. Sci.*, vol. 281, no. 1795, 2014, Art. no. 20141742.
[5] S. R. Freitas, T. J. Hawbaker, and J. P. Metzger, "Effects of roads, topography, and land use on forest cover dynamics in the brazilian atlantic forest," *Forest Ecol. Manage.*, vol. 259, no. 3, pp. 410–417, 2010.

[6] C. X. Garzon-Lopez, S. A. Bohlman, H. Olff, and P. A. Jansen, "Mapping tropical forest trees using high-resolution aerial digital photographs," *Biotropica*, vol. 45, no. 3, pp. 308–316, 2013.

[7] S. Soltani, O. Ferlian, N. Eisenhauer, H. Feilhauer, and T. Kattenborn, "From simple labels to semantic image segmentation: Leveraging citizen science plant photographs for tree species mapping in drone imagery," *EGUsphere*, vol. 2023, pp. 1–37, 2023.

[8] R. Valencia, H. Balslev, and G. Paz Y Miño C,, "High tree alpha-diversity in Amazonian Ecuador," *Biodiversity Conservation*, vol. 3, pp. 21–28, 1994.

[9] S. Guitet, O. Brunaux, and J.-F. Molino, "Diversité et écologie des arbres en forêt guyanaise," in *Guide des arbres de Guyane*. H. Richard and J. Ateni, Eds., Cayenne, Guyane Française: Office National des Forêts, 3rd ed., 2022, pp. 34–45.

[10] P. Ghamisi, J. Plaza, Y. Chen, J. Li, and A. J. Plaza, "Advanced spectral classifiers for hyperspectral images: A review," *IEEE Geosci. Remote Sens. Mag.*, vol. 5, no. 1, pp. 8–32, Mar. 2017.

[11] M. L. Clark, D. A. Roberts, and D. B. Clark, "Hyperspectral discrimination of tropical rain forest tree species at leaf to crown scales," *Remote Sens. Environ.*, vol. 96, no. 3/4, pp. 375–398, 2005.

[12] A. Laybros et al., "Across date species detection using airborne imaging spectroscopy," *Remote Sens.*, vol. 11, no. 7, 2019, Art. no. 789.

[13] M. Wietecha, Ł. Jełowicki, K. Mitelsztedt, S. Miścicki, and K. Stereńczak, "The capability of species-related forest stand characteristics determination with the use of hyperspectral data," *Remote Sens. Environ.*, vol. 231, 2019, Art. no. 111232.

[14] W. Jia, Y. Pang, R. Tortini, D. Schläpfer, Z. Li, and J.-L. Roujean, "A kernel-driven BRDF approach to correct airborne hyperspectral imagery over forested areas with rugged topography," *Remote Sens.*, vol. 12, no. 3, 2020, Art. no. 432.

[15] M. S. Colgan, C. A. Baldeck, J.-B. Féret, and G. P. Asner, "Mapping savanna tree species at ecosystem scales using support vector machine classification and BRDF correction on airborne hyperspectral and lidar data," *Remote Sens.*, vol. 4, no. 11, pp. 3462–3480, 2012.

[16] W. Jia, Y. Pang, and R. Tortini, "The influence of BRDF effects and representativeness of training data on tree species classification using multi-flightline airborne hyperspectral imagery," *ISPRS J. Photogrammetry Remote Sens.*, vol. 207, pp. 245–263, 2024.

[17] J. Theiler, A. Ziemann, S. Matteoli, and M. Diani, "Spectral variability of remotely sensed target materials: Causes, models, and strategies for mitigation and robust exploitation," *IEEE Geosci. Remote Sens. Mag.*, vol. 7, no. 2, pp. 8–30, Jun. 2019.

[18] R. A. Borsoi et al., "Spectral variability in hyperspectral data unmixing: A comprehensive review," *IEEE Geosci. Remote Sens. Mag.*, vol. 9, no. 4, pp. 223–270, Dec. 2021.

[19] G. P. Asner, "Biophysical and biochemical sources of variability in canopy reflectance," *Remote Sens. Environ.*, vol. 64, no. 3, pp. 234–253, 1998.

[20] S. Jacquemoud and F. Baret, "Prospect: A model of leaf optical properties spectra," *Remote Sens. Environ.*, vol. 34, no. 2, pp. 75–91, 1990.

[21] J.-B. Féret, A. Gitelson, S. Noble, and S. Jacquemoud, "PROSPECT-D: Towards modeling leaf optical properties through a complete lifecycle," *Remote Sens. Environ.*, vol. 193, pp. 204–215, 2017.

[22] W. Verhoef, "Light scattering by leaf layers with application to canopy reflectance modeling: The sail model," *Remote Sens. Environ.*, vol. 16, no. 2, pp. 125–141, 1984.

[23] S. Jacquemoud et al., "PROSPECT SAIL models: A review of use for vegetation characterization," *Remote Sens. Environ.*, vol. 113, pp. S56–S66, 2009.

[24] S. V. Ollinger, "Sources of variability in canopy reflectance and the convergent properties of plants," *New Phytologist*, vol. 189, no. 2, pp. 375–394, 2011.

[25] J. G. C. Ball et al., "Harnessing temporal and spectral dimensionality to map and identify species of individual trees in diverse tropical forests," Cold Spring Harbor Laboratory, Jun. 2024.

[26] R. Richter and D. Schläpfer, "Atmospheric and topographic correction (ATCOR theoretical background document)," ReSe Applications LLC, Wil, Switzerland, Tech. Rep. DLR-IB 564-03/2023, 2023.

[27] G. P. Anderson et al., "Modtran4-based atmospheric correction algorithm: Flaash (fast line-of-sight atmospheric analysis of spectral hypercubes)," in *Algorithms Technologies Multispectral, Hyperspectral, Ultraspectral Imagery VIII*, Bellingham, WA, USA: SPIE, 2002, vol. 4725, pp. 65–71.

[28] D. R. Thompson, V. Natraj, R. O. Green, M. C. Helmlinger, B.-C. Gao, and M. L. Eastwood, "Optimal estimation for imaging spectrometer atmospheric correction," *Remote Sens. Environ.*, vol. 216, pp. 355–373, 2018.

[29] D. R. Thompson et al., "Retrieval of atmospheric parameters and surface reflectance from visible and shortwave infrared imaging spectroscopy data," *Surv. Geophys.*, vol. 40, pp. 333–360, 2019.

[30] J. P. Arroyo-Mora et al., "Assessing the impact of illumination on UAV pushbroom hyperspectral imagery collected under various cloud cover conditions," *Remote Sens. Environ.*, vol. 258, 2021, Art. no. 112396.

[31] D. Schläpfer, R. Richter, and T. Feingersh, "Operational BRDF effects correction for wide-field-of-view optical scanners (BREFCOR)," *IEEE Trans. Geosci. Remote Sens.*, vol. 53, no. 4, pp. 1855–1864, Apr. 2015.

[32] F. de Boissieu et al., "Validation of the DART model for airborne laser scanner simulations on complex forest environments," *IEEE J. Sel. Topics Appl. Earth Observ. Remote Sens.*, vol. 16, pp. 8379–8394, 2023.

[33] R. Montes and C. Ureña, "An overview of BRDF models," Univ. Granada, True Blue, Grenada, Tech. Rep. LSI-2012, 2012, vol. 1.

[34] I. Korpela, V. Heikkinen, E. Honkavaara, F. Rohrbach, and T. Tokola, "Variation and directional anisotropy of reflectance at the crown scale–implications for tree species classification in digital aerial images," *Remote Sens. Environ.*, vol. 115, no. 8, pp. 2062–2074, 2011.

[35] D. Kükenbrink et al., "Mapping the irradiance field of a single tree: Quantifying vegetation-induced adjacency effects," *IEEE Trans. Geosci. Remote Sens.*, vol. 57, no. 7, pp. 4994–5011, Jul. 2019.

[36] M. Vögtli, D. Schläpfer, M. C. Schuman, M. E. Schaepman, M. Kneubühler, and A. Damm, "Effects of atmospheric, topographic, and BRDF correction on imaging spectroscopy-derived data products," *IEEE J. Sel. Topics Appl. Earth Observ. Remote Sens.*, vol. 17, pp. 109–126, 2024.

[37] C. A. Baldeck et al., "Operational tree species mapping in a diverse tropical forest with airborne imaging spectroscopy," *PLoS One*, vol. 10, no. 7, 2015, Art. no. e0118403.

[38] D. Schläpfer, R. Richter, and A. Damm, "Correction of shadowing in imaging spectroscopy data by quantification of the proportion of diffuse illumination," in *Proc. 8th SIG-IS EARSeL Imag. Spectrosc. Workshop*, 2013, pp. 8–13.

[39] G. Zhang, D. Cerra, and R. Müller, "Shadow detection and restoration for hyperspectral images based on nonlinear spectral unmixing," *Remote Sens.*, vol. 12, no. 23, 2020, Art. no. 3985.

[40] N. Carmon et al., "Shape from spectra," *Remote Sens. Environ.*, vol. 288, 2023, Art. no. 113497.

[41] A. Berk et al., "Modtran 5: A reformulated atmospheric band model with auxiliary species and practical multiple scattering options: Update," in *Proc. 11th Algorithms Technol. Multispectral, Hyperspectral, Ultraspectral Imagery*, 2005, vol. 5806, pp. 662–667.

[42] S. T. Brantley, J. C. Zinnert, and D. R. Young, "Application of hyperspectral vegetation indices to detect variations in high leaf area index temperate shrub thicket canopies," *Remote Sens. Environ.*, vol. 115, no. 2, pp. 514–523, 2011.

[43] P. Launeau et al., "Airborne hyperspectral mapping of trees in an urban area," *Int. J. Remote Sens.*, vol. 38, no. 5, pp. 1277–1311, 2017.

[44] J. W. Rouse et al., "Monitoring vegetation systems in the great plains with ERTs," *NASA Spec. Publ*, vol. 351, no. 1, 1974, Art. no. 309.

[45] F. D. Schneider et al., "Mapping functional diversity from remotely sensed morphological and physiological forest traits," *Nature Commun.*, vol. 8, no. 1, 2017, Art. no. 1441.

[46] A. A. Gitelson, G. P. Keydan, and M. N. Merzlyak, "Three-band model for noninvasive estimation of chlorophyll, carotenoids, and anthocyanin contents in higher plant leaves," *Geophysical Res. Lett.*, vol. 33, no. 11, 2006, L11402.

[47] E. Underwood, S. Ustin, and D. DiPietro, "Mapping nonnative plants using hyperspectral imagery," *Remote Sens. Environ.*, vol. 86, no. 2, pp. 150–161, 2003.

[48] S. Gourlet-Fleury, J.-M. J.-M. Guehl, and O. Laroussinie, "Ecology and management of a neotropical rainforest," in *Lessons Drawn From Paracou, a Long-Term Experimental Research Site in French Guiana*. Amsterdam, Netherlands: Elsevier, 2004.

[49] F. Bongers, *Nouragues: Dynamics and Plant-Animal Interactions in a Neotropical Rainforest*, vol. 80. Berlin, Germany: Springer, 2001.

[50] D. Schläpfer, "PARGE - parametric geocoding, version 4.0," ReSe Applications LLC, 2024. [Online]. Available: http://www.parge.com

[51] N. Bhatia, M.-D. Iordache, A. Stein, I. Reusen, and V. A. Tolpekin, "Propagation of uncertainty in atmospheric parameters to hyperspectral unmixing," *Remote Sens. Environ.*, vol. 204, pp. 472–484, 2018.

[52] D. Schläpfer, A. Hueni, and R. Richter, "Cast shadow detection to quantify the aerosol optical thickness for atmospheric correction of high spatial resolution optical imagery," *Remote Sens.*, vol. 10, no. 2, p. 200, 2018.

[53] D. Scheffler, A. Hollstein, H. Diedrich, K. Segl, and P. Hostert, "AROSICS: An automated and robust open-source image co-registration software for multi-sensor satellite data," *Remote Sens.*, vol. 9, no. 7, 2017, Art. no. 676.
[54] R. J. Tibshirani and B. Efron, "An introduction to the bootstrap," *Monographs Statist. Appl. Probability*, vol. 57, no. 1, 1993.
[55] N. Pettorelli, *The Normalized Difference Vegetation Index*. Oxford, U.K.: Oxford Univ. Press, 2013.
[56] S. S. Park, S.-W. Kim, C.-K. Song, J.-U. Park, and K.-H. Bae, "Spatio-temporal variability of aerosol optical depth, total ozone and NO_2 over east Asia: Strategy for the validation to the gems scientific products," *Remote Sens.*, vol. 12, no. 14, 2020, Art. no. 2256.
[57] J. Kim et al., "New era of air quality monitoring from space: Geostationary environment monitoring spectrometer (GEMS)," *Bull. Amer. Meteorological Soc.*, vol. 101, no. 1, pp. E1–E22, 2020.
[58] H. Vogelmann, R. Sussmann, T. Trickl, and A. Reichert, "Spatio-temporal variability of water vapor investigated by LiDAR and FTIR vertical soundings above Mt. Zugspitze," *Atmos. Chem. Phys. Discuss*, vol. 14, pp. 28231–28268, 2014.
[59] W. J. Shuttleworth, "Evaporation from amazonian rainforest," in *Proc. Roy. Soc. London. Ser. B. Biol. Sci.*, vol. 233, no. 1272, pp. 321–346, 1988.
[60] C. Kocha, P. Tulet, J.-P. Lafore, and C. Flamant, "The importance of the diurnal cycle of aerosol optical depth in West Africa," *Geophysical Res. Lett.*, vol. 40, no. 4, pp. 785–790, 2013.
[61] N. Yokoya, N. Miyamura, and A. Iwasaki, "Preprocessing of hyperspectral imagery with consideration of smile and keystone properties," in *Proc. Multispectral, Hyperspectral, Ultraspectral Remote Sens. Technol. Techn. Appl. III*, 2010, vol. 7857, pp. 73–81.
[62] Y. Chang, L. Yan, H. Fang, and C. Luo, "Anisotropic spectral-spatial total variation model for multispectral remote sensing image destriping," *IEEE Trans. Image Process.*, vol. 24, no. 6, pp. 1852–1866, Jun. 2015.
[63] Y. Guo, J. Senthilnath, W. Wu, X. Zhang, Z. Zeng, and H. Huang, "Radiometric calibration for multispectral camera of different imaging conditions mounted on a UAV platform," *Sustainability*, vol. 11, no. 4, 2019, Art. no. 978.
[64] B.-C. Gao, M. J. Montes, C. O. Davis, and A. F. Goetz, "Atmospheric correction algorithms for hyperspectral remote sensing data of land and ocean," *Remote Sens. Environ.*, vol. 113, pp. S17–S24, 2009.
[65] G. Doxani et al., "Atmospheric correction inter-comparison exercise, acix-ii land: An assessment of atmospheric correction processors for landsat 8 and sentinel-2 over land," *Remote Sens. Environ.*, vol. 285, 2023, Art. no. 113412.
[66] D. Schläpfer, C. C. Borel, J. Keller, and K. I. Itten, "Atmospheric precorrected differential absorption technique to retrieve columnar water vapor," *Remote Sens. Environ.*, vol. 65, no. 3, pp. 353–366, 1998.
[67] R. de Los Reyes et al., "PACO: Python-based atmospheric correction," *Sensors*, vol. 20, no. 5, 2020, Art. no. 1428.
[68] C. A. Petri and L. S. Galvão, "Sensitivity of seven MODIS vegetation indices to BRDF effects during the amazonian dry season," *Remote Sens.*, vol. 11, no. 14, 2019, Art. no. 1650.
[69] L. S. Galvão, C. Arlanche Petri, and R. Dalagnol, "Coupled effects of solar illumination and phenology on vegetation index determination: An analysis over the amazonian forests using the superdove satellite constellation," *GIScience Remote Sens.*, vol. 61, no. 1, 2024, Art. no. 2290354.
[70] M. D. Cross, T. Scambos, F. Pacifici, and W. E. Marshall, "Determining effective meter-scale image data and spectral vegetation indices for tropical forest tree species differentiation," *IEEE J. Sel. Topics Appl. Earth Observ. Remote Sens.*, vol. 12, no. 8, pp. 2934–2943, Aug. 2019.
[71] R. B. Myneni et al., "Large seasonal swings in leaf area of amazon rainforests," in *Proc. Nat. Acad. Sci.*, vol. 104, no. 12, pp. 4820–4823, 2007.
[72] D. C. Morton et al., "Amazon forests maintain consistent canopy structure and greenness during the dry season," *Nature*, vol. 506, no. 7487, pp. 221–224, 2014.
[73] R. da Silva Palácios et al., "Long term analysis of optical and radiative properties of aerosols in the amazon basin," *Aerosol Air Qual. Res.*, vol. 20, no. 1, pp. 139–154, 2020.
[74] D. Inamdar, M. Kalacska, J. P. Arroyo-Mora, and G. Leblanc, "The directly-georeferenced hyperspectral point cloud: Preserving the integrity of hyperspectral imaging data," *Front. Remote Sens.*, vol. 2, 2021, Art. no. 675323.
[75] A. I. Lyapustin et al., "Multi-angle implementation of atmospheric correction for MODIS (MAIAC): 3. atmospheric correction," *Remote Sens. Environ.*, vol. 127, pp. 385–393, 2012.

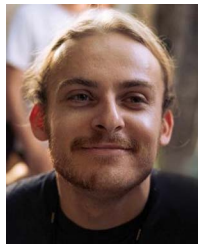

Colin Prieur received the graduation degree in data science from Grenoble INP, Grenoble, France, in 2022. He is currently working toward the Ph.D. degree in remote sensing with the University of Montpellier, Montpellier, France.

In 2020, as part of an internship with Helwett Packard Entreprise, he organized the Detection of Settlements without Electricity track of the 2021 edition of the IEEE GRSS data-fusion contest. In 2021, he spent four month as a Visiting Researcher with the Colourlab, Gjøvik, Norway, to study methods for glacier monitoring using remote sensing multispectral satellite and machine learning methods. In 2022, he spent six month for a research internship with CESBIO laboratory. His research interests include forestry, optical remote sensing, machine learning, artificial intelligence and their development as operational methods.

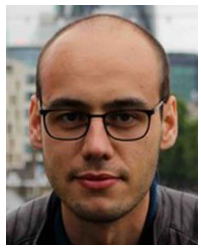

Antony Laybros received the M.Sc. degree in remote sensing from Université de Rennes 2, Rennes, France, in 2016, and the Ph.D. degree in ecology and remote sensing from the Université de Montpellier, France, in 2021.

His research interests include tropical forest, hyperspectral imagery, LiDAR point clouds, and machine learning methods, including deep learning methods. The development of operational methods in these different fields and their routine applications is also one of its aspirations.

Giovanni Frati received the degree in geosciences in 2015 from the University of La Rochelle, France, and research master's degree in planetary science from the University of Nantes, France, in 2018, and a Ph.D. in remote sensing and geosciences from the Planetology and Geosciences Laboratory at the University of Nantes, France, in 2021.

He worked on synchronized full-waveform LiDAR and hyperspectral imaging for monitoring the dynamics of sandy coastlines with the Planetology and Geosciences Laboratory. After completing the Ph.D., he joined GEOFIT, where he helped advance hyperspectral technology, notably through a French-Chilean collaboration aimed at monitoring native Chilean forests using hyperspectral imaging. He later transitioned to the IRD, where he now works as a Research Engineer specialized in forest hyperspectral remote sensing.

Daniel Schläpfer (Member, IEEE) received the M.Sc. degree in geography and atmospheric physics and the Ph.D. (Dr.Sc.Nat.) degree in remote sensing from the University of Zürich, Zürich, Switzerland, in 1994 and 1998, respectively, and the Teaching Professor degree in physics from the Education Department of Canton, St. Gallen, Switzerland, in 2009.

He is currently a Physics Teacher with Kantonsschule, Wil, Switzerland, and is also working with ReSe Applications LLC, Wil. His research interests include the geometric preprocessing of airborne scanner data on the basis of the PARGE software, the application of radiative transfer models in imaging spectroscopy, and the advancement of radiometric and atmospheric compensation in the framework of the ATCOR and DROACOR atmospheric correction solutions.

Jocelyn Chanussot (Fellow, IEEE) received the M.Sc. degree in electrical engineering from the Grenoble Institute of Technology (Grenoble INP), Grenoble, France, in 1995, and the Ph.D. degree from the Université de Savoie, Annecy, France, in 1998.

From 1999 to 2023, he has been with Grenoble INP, where he was a Professor of signal and image processing. He is currently a Research Director with INRIA, Grenoble. His research interests include image analysis, hyperspectral remote sensing, data fusion, machine learning, and artificial intelligence. He has been a Visiting Scholar with Stanford University, Stanford, CA, USA, KTH, Stockholm, Sweden, and NUS, Singapore. Since 2013, he has been an Adjunct Professor with the University of Iceland, Reykjavik, Iceland. From 2015 to 2017, he was a Visiting Professor with the University of California, Los Angeles (UCLA). He is an Adjunct Professor with the Chinese Academy of Sciences, Aerospace Information Research Institute, Beijing.

Dr. Chanussot holds the AXA Chair in remote sensing. He is the founding President of IEEE Geoscience and Remote Sensing French chapter (2007–2010) which received the 2010 IEEE GRS-S Chapter Excellence Award. He has received multiple outstanding paper awards. He was the Vice-President of the IEEE Geoscience and Remote Sensing Society, in charge of meetings and symposia (2017–2019). He was the General Chair of the first IEEE GRSS Workshop on Hyperspectral Image and Signal Processing, Evolution in Remote sensing (WHISPERS). He was the Chair (2009–2011) and the Cochair of the GRS Data Fusion Technical Committee (2005–2008). He was a Member of the Machine Learning for Signal Processing Technical Committee of the IEEE Signal Processing Society (2006–2008) and the Program Chair of the IEEE International Workshop on Machine Learning for Signal Processing (2009). He is an Associate Editor for IEEE TRANSACTIONS ON GEOSCIENCE AND REMOTE SENSING, IEEE TRANSACTIONS ON IMAGE PROCESSING, and the *Proceedings of the IEEE*. He was the Editor-in-Chief of *IEEE Journal of Selected Topics in Applied Earth Observations and Remote Sensing* (2011–2015). In 2014. he served as a Guest Editor for the *IEEE Signal Processing Magazine*. He is an ELLIS Fellow, a Fellow of the Asia-Pacific Artificial Intelligence Association, a Member of the Institut Universitaire de France (2012–2017) and a Highly Cited Researcher (Clarivate Analytics/Thomson Reuters, since 2018).

Grégoire Vincent received the M.Sc. degree in agronomy from the Institut National Polytechnique de Lorraine, Vandoeuvre les Nancy, France, in 1989, and the Ph.D. degree in systems modeling from Université de Lyon, Lyon, France, in 1993.

He is a Forest Ecologist. His current research interests include leveraging new remote sensing technologies to improve our understanding of tropical forest response to ongoing climate change.